Electrophysiological Brain Source Imaging via Combinatorial Search with Provable Optimality

Guihong Wan[1], Meng Jiao[2], Xinglong Ju[3], Yu Zhang[4], Haim Schweitzer[5], Feng Liu[2*]

[1] Massachusetts General Hospital, Harvard Medical School
[2] School of Systems and Enterprises, Stevens Institute of Technology
[3] Division of Management Information Systems, The University of Oklahoma
[4] Department of Bioengineering, Lehigh University
[5] Department of Computer Science, The University of Texas at Dallas
gwan@mgh.harvard.edu, mjiao@stevens.edu, xinglong.ju@ou.edu
yuzi20@lehigh.edu, hschweitzer@utdallas.edu, fliu22@stevens.edu

Abstract

Electrophysiological Source Imaging (ESI) refers to reconstructing the underlying brain source activation from non-invasive Electroencephalography (EEG) and Magnetoencephalography (MEG) measurements on the scalp. Estimating the source locations and their extents is a fundamental tool in clinical and neuroscience applications. However, the estimation is challenging because of the ill-posedness and high coherence in the leadfield matrix as well as the noise in the EEG/MEG data. In this work, we proposed a combinatorial search framework to address the ESI problem with a provable optimality guarantee. Specifically, by exploiting the graph neighborhood information in the brain source space, we converted the ESI problem into a graph search problem and designed a combinatorial search algorithm under the framework of A^* to solve it. The proposed algorithm is guaranteed to give an optimal solution to the ESI problem. Experimental results on both synthetic data and real epilepsy EEG data demonstrated that the proposed algorithm could faithfully reconstruct the source activation in the brain.

Introduction

Neuronal firing and interactions between neural circuits at different brain regions serve as a fundamental mechanism for brain sensory and cognitive functions. The brain physiological and cognitive behaviors generate electromagnetic and metabolic signals that can be measured with different neuroimaging modalities. Typically, these modalities are classified into two categories: (i) invasive measurement modalities, such as stereoelectroencephalography (sEEG) (Iida and Otsubo 2017) and electrocorticography (ECoG) (Keene, Whiting, and Ventureyra 2000); (ii) non-invasive measurement modalities, such as Electroencephalogram (EEG) and Magnetoencephalogram (MEG) (Cuffin and Cohen 1979; Phillips, Rugg, and Friston 2002), functional magnetic resonance imaging (fMRI) (Huettel et al. 2004), positron emission tomography (PET) (Muehllehner and Karp 2006), and single-photon emission computed tomography (SPECT) (He et al. 2018). EEG/MEG directly measures electrical firing patterns between neurons. In contrast, fMRI, another important non-invasive brain imaging modality, measures the blood-oxygen-level-dependent (BOLD) signal that is a secondary metabolic signal (Liu et al. 2022). EEG/MEG provides uniquely high temporal resolution at the millisecond scale for underlying brain activities and contains rich information about brain function and dysfunction, making EEG/MEG studies highly valuable for clinical, cognitive, and behavioral brain investigations.

Electrophysiological Source Imaging (ESI), also known as EEG/MEG Source Localization, is a non-invasive neuroimaging technology used to reconstruct the brain source activation from EEG/MEG measurements, utilizing a head model to characterize the effect of volume conduction or field propagation (He and Ding 2013; Yang et al. 2016; Liu et al. 2017; He et al. 2018; Guo et al. 2022). In some event-related experimental designs, a reasonable assumption is that only a small fraction of the brain sources is consistently activated (Gramfort et al. 2013), implying that ESI solutions for such experiments are spatially sparse (Babadi et al. 2014; Costa et al. 2015). In addition, the brain source activation has a temporal structure that can be exploited to improve ESI performance, such as using a state-space model (Pirondini et al. 2017) or a temporal smooth regularization (Qin et al. 2017; Liu et al. 2018).

The accurate estimation of *the activated area*, including the sources and their extents, is crucial for detecting the location and size of the epileptogenic zone (Ding, Wilke, and *et al.* 2007; Sohrabpour and He 2021; Sun et al. 2022). To improve the accuracy and spatial smoothness of ESI, many studies leveraged the spatial structure of the source signal, such as using the total variation (TV) defined in the source space (Ding and He 2008) and using a predefined Gaussian kernel (Haufe et al. 2011; Liu et al. 2020). The TV regularization defined on the irregular 3D brain mesh can help render an extended source activation pattern. However, the transformation matrix can regulate the activation pattern of the source signal; for example, it promotes the same signal magnitude in the neighboring source space. As a result, using a TV regularization provides a sub-optimal solution and is not flexible to capture the complicated activation pattern.

*Corresponding author.

In this work, we presented a combinatorial search approach to addressing the ESI problem in neuroscience. Instead of imposing a TV regularization term in the objective function, we directly employed the neighborhood connectivity structure in the brain source space to enforce the spatial smoothness of the activation pattern. Specifically, we reformulated the original ESI problem into a graph search problem of the leadfield matrix and introduced a combinatorial search framework in a setting similar to the A* algorithm, which is optimized to provide a provably optimal solution. Our main contributions are summarized as follows:

- We converted the ESI problem into a column search problem of the leadfield matrix.
- We described a combinatorial search framework with a provable optimality guarantee to address the problem.
- Extensive experimental results demonstrated the effectiveness of the proposed approach.

The code: https://github.com/ghwanlab/ESI-AStar.

The EEG/MEG Source Imaging Problem

EEG/MEG measures electromagnetic signals generated from neuronal activities in the brain. The relationship between the source signal activation and the EEG/MEG measurements is characterized by a linear mapping matrix called a leadfield matrix or a head model. The ESI forward model can be expressed as follows:

$$X = L\Phi + E, \tag{1}$$

where $X \in \mathbb{R}^{c\times\tau}$ represents the EEG/MEG data, c is the number of EEG/MEG channels, τ is the number of time points, $L \in \mathbb{R}^{c\times m}$ is the leadfield matrix, m is the number of brain sources, $\Phi \in \mathbb{R}^{m\times\tau}$ represents the electrical potentials in the source space for all the τ time points, and E is the noise in the EEG/MEG channels. Since the number of channels c is much smaller than the number of sources m, estimating Φ becomes ill-posed and has infinite solutions. Thus, regularization terms based on prior assumptions are commonly used:

$$\min_{\Phi} \|X - L\Phi\|_F^2 + \lambda R(\Phi). \tag{2}$$

The first term is the data fitting term to find Φ to explain the observed EEG/MEG data, and the second term is the regularization term to address the ill-posedness property of the ESI problem while promoting a neurophysiologically plausible solution. The widely used options include ℓ_1 norm for the Minimum Current Estimation (MCE) algorithm (Uutela, Hämäläinen, and Somersalo 1999), ℓ_2 norm for the Minimum Norm Estimate (MNE) algorithm (Hämäläinen and Ilmoniemi 1994) and its variants, such as sLORETA (Pascual-Marqui 2002) and dSPM (Dale et al. 2000).

To promote a preference for an extended area of source reconstruction, both TV regularization and sparsity regularization are reasonable choices (Xu et al. 2021). Then, the objective function is given as follows:

$$\min_{\Phi} \|X - L\Phi\|_F^2 + \alpha \|V\Phi\|_1 + \beta \|\Phi\|_1, \tag{3}$$

where V is the discrete gradient operator (Ding and He 2008; Sohrabpour et al. 2020). However, including TV regularization in the objective function can sometimes render unexpected results, as shown in Section 2.2 of (Liu et al. 2022). This observation motivates us to develop an algorithm that directly leverages the spatial connectivity structure in the brain source space for reconstructing an extended and focal source activation pattern.

We assume that the brain source activation is sparse in the cortex, which is a reasonable assumption under the event-related potential (ERP) paradigm (Gramfort, Kowalski, and Hämäläinen 2012). Let k be the number of activated sources corresponding to k columns in the leadfield matrix L. If the k activated columns of L, referred to as S, are known, then estimating the source potential A is trivial:

$$e(S) = \min_{A} \|X - SA\|_F^2, \tag{4}$$

where $S \in \mathbb{R}^{c\times k}$ is constructed from k columns of L, and $A \in \mathbb{R}^{k\times\tau}$ is the source potential corresponding to the k nonzero rows of Φ in Eq. (2). When S is known, A can be derived from $A = S^+X$, where S^+ is the pseudo-inverse of S (Marshall, Olkin, and Arnold 2011). Thus, the ESI problem can be viewed as a column selection problem, which is to identify k columns from L to represent X such that the error in Eq. (4) is minimized.

In the EEG/MEG source space, all potential sources are represented by vertices defined on a tessellated triangular mesh of the brain, as illustrated in Figure 1. When a vertex is activated, its neighbors are also activated with a high likelihood, as the brain tissues serve as electrical conductors for the electromagnetic signal. Thus, the identified columns in S are expected to be connected. As shown by Liu et al. (2022), total variation regularization may not always provide desirable solutions. In this work, a search graph based on the neighborhood of brain sources is constructed and utilized to identify the connected activated area. To avoid ambiguity, we refer to the brain mesh and its vertices as "mesh" and "vertices", and the graph for combinatorial search and its nodes as "graph" and "nodes".

The Proposed Optimization Framework

Combinatorial Search

A^* (Hart, Nilsson, and Raphael 1968) is a classic combinatorial search framework, which has been widely used in graph traversal and path search. The first step is to model the problem as a graph search problem, and then the best-first strategy is used to guide the search for a path from a root node to a goal node, which minimizes the cost. In general, two lists of nodes are maintained: (i) a fringe list, containing nodes that have been generated but not yet expanded; (ii) a closed list, containing all expanded nodes to avoid revisiting.

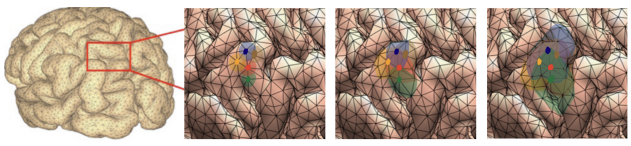

Figure 1: Illustration of a brain mesh and the 0/1/2-level neighborhood activation of brain sources.

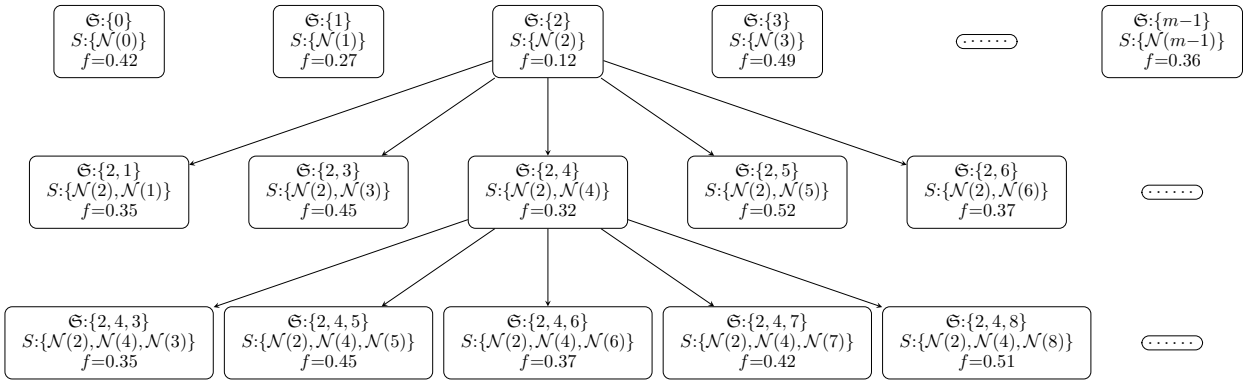

Figure 2: An example of search graph for 1-level neighborhood activation, where $\mathcal{N}(v, l)$ is simplified as $\mathcal{N}(v)$. $\mathcal{N}(2) = \{2, 1, 3, 4, 5, 6\}$ and $\mathcal{N}(4) = \{4, 2, 3, 5, 6, 7, 8\}$. The f values are used to guide the search.

Each node on the search graph has a heuristic value based on an approximate cost of a least-cost path. In each iteration, the node with the smallest heuristic value in the fringe list is picked and expanded until a goal node is found. With certain conditions on heuristics, A^* is guaranteed to find an optimal solution. Recent studies have applied A^* and its weighted variants to address important problems in data science, such as robust principal component analysis (Wan and Schweitzer 2021a), and unsupervised feature selection (He et al. 2019). The algorithm we propose in this work is based on the standard A^* algorithm and customized for the ESI problem.

Search Graph for the ESI Problem

In this section, we show how to construct the search graph for the ESI problem. Suppose each vertex on the brain mesh is indexed from 0 to $m-1$ corresponding to the m columns in the leadfield matrix L. Let $\mathcal{N}(v, l)$ be a function that outputs the neighbors of any vertex v (including itself) with the neighborhood level $\leq l$. Now we can build the search graph starting by creating m nodes at the root level corresponding to the m vertices. As shown in Figure 2, a node consists of a set $\mathfrak{S}$, a set S, and a heuristic value f. The set $\mathfrak{S}$ contains main activated vertices, the set S contains neighbors of all main activated vertices based on l-level neighborhood activation, and the heuristic value f is based on the error defined in Eq. (4), which will be defined later. Children of a node are created by adding a new vertex on the mesh into the parent-level $\mathfrak{S}$ and the corresponding neighbors of this vertex into the parent-level S. To promote spatial continuity of an activated area, only the vertices in S at the parent level can be used to create children. A goal node is a node with S containing k vertices. With slightly ambiguous use of notation, both the vertex set and the submatrix of L containing the corresponding columns are denoted as S.

Unlike search graphs for the standard A^*, which starts with a root node, we start from m nodes corresponding to all vertices on the brain mesh. Another difference is that the order of vertices in $\mathfrak{S}$ and S is irrelevant. For example, a node with $\mathfrak{S}$=$\{2, 4\}$ is equivalent to a node with $\mathfrak{S}$=$\{4, 2\}$ and the heuristic values for them are same. When one of them is created, we do not need to create another.

Algorithm 1: The ESI-A^* Algorithm.

Input: X: EEG/MEG data matrix. L: the leadfield matrix. k: the desired number of vertices of an activated area. $\mathcal{N}(v, l)$: the neighborhood function for a vertex v and the desired l-level neighborhood activation. $f(S)$: a heuristic function to compute the heuristic value f for a node n with S to guide the search.
Output: A solution set S consisting of k activated vertices.
Initialization: Add the m nodes at the root level (corresponding to all vertices on the brain mesh) into the Fringe list F and the Closed list C.
Procedure:

1: **while** $F \neq \emptyset$ **do**
2: Find node n_p (containing $\mathfrak{S}_p$ and S_p) with the smallest heuristic value f_p from F. Ties are resolved by choosing the node with more vertices in S_p.
3: Remove node n_p from F.
4: **if** n_p is a goal node (S_p contains k vertices) **then**
5: Return S_p as the solution.
6: **else**
7: **for** each child n_i of n_p **such that** $n_i \notin C$ **do**
8: compute the heuristic value f_i for n_i.
9: put n_i into F and C.
10: **end for**
11: **end if**
12: **end while**

The Combinatorial Search Algorithm

The search algorithm defined on the search graph for the ESI problem is described in Algorithm 1. It is similar to the standard A^* and we refer to it as "ESI-A^*". The heuristic function based on the error Eq. (4) is used to guide the search.

When a node at the parent level n_p is picked up at Line 2, it will be expanded for a bigger activated area by creating its children according to the l-level neighborhood activation. In the next iteration, one of its children or another potentially promising node is selected and expanded. Guided by the heuristic values, only the promising nodes, not all nodes, are expanded. In the end, an activated area of k vertices is

found. Note that when $l>0$, in each iteration S is expanded by adding one or more vertices. For example, if a vertex on the brain mesh has 7 neighbors (including itself), when $l=1$ in each iteration S can grow larger by adding 1, 2, or 3 vertices. (At least 4 neighbors must be already included.) Therefore, an activated area of exact k vertices may not exist. To deal with this, we can add tolerance for k or simply run the algorithm with another k value. Since the order of vertices in $\mathfrak{S}$ and S is irrelevant, Line 9 puts a node into F and C simultaneously such that C is a superset of F.

We proceed to define the heuristic function and show that ESI-A^* is guaranteed to find an optimal solution for a given l-level neighborhood activation.

The Heuristic Function

The goal of the ESI-A^* algorithm is to detect a node with a set S containing k connected vertices representing an activated area in the brain such that the error defined in (4) is minimized. Given a node n_i with S_i of size k_i on the search graph, define e_{exact} as the minimum error if these k_i vertices in S_i are included in the final solution. This means we need to complete S_i from k_i to k:

$$e_{\text{exact}}(S_i) = \min_{S_j, A_i, A_j} \|X - S_i A_i - S_j A_j\|_F^2, \qquad (5)$$

where S_j contains $k - k_i$ vertices, A_i and A_j are the coefficient matrices. It is easy to prove that using $e_{\text{exact}}(S_i)$ as the heuristic function, ESI-A^* is optimal. However, it is challenging to compute $e_{\text{exact}}(S_i)$ efficiently as finding S_j can be viewed as an ESI problem on the reduced X and L by S_i. We approximate it by a lower bound:

$$e_{\text{lower}}(S_i) = \min_{U, A_i, A_u} \|X - S_i A_i - U A_u\|_F^2, \qquad (6)$$

where $U \in \mathbb{R}^{c \times (k-k_i)}$ contains $k-k_i$ unconstrained vectors (not necessarily from L), and A_u is the coefficient matrix. By relaxing the condition on S_j (must be a submatrix of L), e_{lower} can be computed efficiently since U formed by the $k - k_i$ left eigenvectors of $X - S_i A_i$ corresponding to the largest $k - k_i$ singular values minimizes the error and $A_i = S_i^+ X$ (Marshall, Olkin, and Arnold 2011). Let $X_i = X - S_i A_i$. Then $e_{\text{lower}}(S_i)$ can be computed as:

$$e_{\text{lower}}(S_i) = \text{trace}(X_i) - \sum_{z=0}^{k-k_i-1} \sigma_z^2, \qquad (7)$$

where $\sigma_0 \geq \cdots \geq \sigma_{k-k_i-1}$ are the largest $k - k_i$ singular values of X_i. See (Wan and Schweitzer 2021c) for proof.

Theorem 1. If $f(S_i) = e_{\text{lower}}(S_i)$, the ESI-$A^*$ algorithm finds an optimal solution for (4).

We are also concerned with adding the spatial smoothness criterion. Let $A^\ddagger$ be the solution in Eq. (4) for a given S. Consider the following error:

$$e(S, \alpha) = e(S) + \alpha |V_k A^\ddagger|_1, \qquad (8)$$

where V_k contains k columns of the discrete gradient operator V corresponding to the k selection of S. Analogously to Eq. (5) at a node n_i we have:

$$e_{\text{exact}}(S_i, \alpha) = e_{\text{exact}}(S_i) + \alpha(|V_i A_i^\ddagger|_1 + |V_j A_j^\ddagger|_1), \qquad (9)$$

where $A_i^\ddagger$ and $A_j^\ddagger$ are the solutions of Eq. (5), V_i, and V_j are the corresponding columns of the discrete gradient operator. We define a lower bound of $e_{\text{exact}}(S_i, \alpha)$ as follows:

$$e_{\text{lower}}(S_i, \alpha) = e_{\text{lower}}(S_i) + \alpha |V_i A_i^\ddagger|_1. \qquad (10)$$

Theorem 2. If $f(S_i, \alpha) = e_{\text{lower}}(S_i, \alpha)$, the ESI-$A^*$ algorithm finds an optimal solution for (8).

When $\alpha = 0$, Eq. (4) is equivalent to Eq. (8). Proofs of Theorem 1 and Theorem 2 are given in the following section.

Optimality of the ESI-A^* Algorithm

The strategy to prove the optimality of the ESI-A^* algorithm (Theorem 1 and Theorem 2) is similar but not identical to the strategy for the optimal variants of the combinatorial search algorithms summarized in (Wan 2021).

Lemma 1. Let S_i be a vertex set of size k_i at a node n_i on the search graph. Then:
i. $e_{\text{lower}}(S_i) \leq e_{\text{exact}}(S_i)$;
ii. if $k = k_i$, then $e_{\text{lower}}(S_i) = e_{\text{exact}}(S_i) = e(S_i)$;
iii. $e_{\text{lower}}(S_i)$ is monotonically increasing along any path.

Proof: For i, from the definition of $e_{\text{lower}}(S_i)$ and $e_{\text{exact}}(S_i)$, it follows that replacing S_j by U with unrestricted columns cannot increase the error. For ii, it is straightforward. For iii, let n_p associated with S_p of size k_p be the parent node of S_i, then we need to prove that $e_{\text{lower}}(S_p) \leq e_{\text{lower}}(S_i)$. Let S_a be $k_i - k_p$ be additional vertices in S_i compared to S_p, then $e_{\text{lower}}(S_i)$ can be written as:

$$\begin{aligned} e_{\text{lower}}(S_i) =& e_{\text{lower}}(S_p \cup S_a) \\ =& \min_{U, A_p, A_a, A_j} \|X - S_p A_p - S_a A_a - U A_j\|_F^2. \end{aligned}$$

Since $e_{\text{lower}}(S_p) = \min_{U_p, A_p, A_j} \|X - S_p A_p - U_p A_j\|_F^2$. It can be viewed as replacing $k_i - k_p$ unrestricted columns in U_p by S_a. Then $e_{\text{lower}}(S_p)$ cannot be less than $e_{\text{lower}}(S_i)$. ■

Lemma 2. Let n_* (associated with S_*) is an optimal node (S_* is an optimal set and $e(S_*)$ is the smallest possible error) for a search graph constructed by using l-level neighborhood activation. Suppose Theorem 1 is false. Then for any node n_g (associated with S_g) on a path from a root node to an optimal goal node, we have: $f(S_g) < f(S)$.

Proof: The falsehood of Theorem 1 can be written as: $e(S) > e(S_*)$. Since S and S_* are both of size k, Lemma 1.ii implies: $e_{\text{lower}}(S) = e(S) = f(S)$, $e_{\text{lower}}(S_*) = e(S_*) = f(S_*)$. Therefore:

$$\begin{aligned} f(S) = e_{\text{lower}}(S) = e(S) > e(S_*) = f(S_*) = e_{\text{lower}}(S_*) \\ \geq e_{\text{lower}}(S_g) = f(S_g), \text{ where } e_{\text{lower}}(S_*) \geq e_{\text{lower}}(S_g), \end{aligned}$$

which is followed from Lemma 1.iii. ■

Lemma 3. During the run of the ESI-A^* algorithm the fringe list F always contains a node n_g that is on the path to an optimal node n_*.

Proof: Straightforward. It can be done by induction. ■

Proof of Theorem 1: The proof is by contradiction. Suppose Theorem 1 is false. From Lemma 3, there is a node n_g (associated with S_g) on the path to an optimal node in the fringe list F. From Lemma 2, $f(S_g) < f(S)$. So the node n_g with S_g will be selected before the solution node with S, which leads to a contradiction. ■

Lemma 4. Let S_i be a vertex set of size k_i at a node n_i on search graph. Then:
i. $e_{\text{lower}}(S_i, \alpha) \leq e_{\text{exact}}(S_i, \alpha)$;
ii. if $k{=}k_i$, then $e_{\text{lower}}(S_i, \alpha) = e_{\text{exact}}(S_i, \alpha) = e(S_i, \alpha)$.
iii. $e_{\text{lower}}(S_i, \alpha)$ is monotonically increasing along any path.

Proof: For i and ii, the proof is straightforward. For iii, let n_p associated with S_p of size k_p be the parent node of S_i, then we need to prove that $e_{\text{lower}}(S_p, \alpha) \leq e_{\text{lower}}(S_i, \alpha)$. Since $e_{\text{lower}}(S_p) \leq e_{\text{lower}}(S_i)$, we need to prove $|V_p A_p^{\ddagger}|_1 \leq |V_i A_i^{\ddagger}|_1$, where $A_p^{\ddagger}$ and $A_i^{\ddagger}$ are the corresponding solutions of Eq. (5), V_p, and V_i are the columns of the discrete gradient operator corresponding to the S_p and S_i. We have: $A_i^{\ddagger} = S_i^{+} X = Q_i^T X$ and $A_p^{\ddagger} = S_p^{+} X = Q_p^T X$, where Q_i and Q_p are the span of S_i and S_p (Marshall, Olkin, and Arnold 2011; Golub and Van Loan 2013). Then:

$$|V_p A_p^{\ddagger}|_1 = |V_p Q_p^T X|_1, |V_i A_i^{\ddagger}|_1 = |V_i Q_i^T X|_1.$$

Since S_i is a column super set of S_p, V_i is a column super set of V_i and Q_i can be formed as a column super set of Q_p. This completes the proof. ■

Proof of Theorem 2: The proof strategy is identical to the one for Theorem 1 and is done by using Lemma 4. ■

Implementation and Complexity

We discuss the implementation of Algorithm 1 with Eq. (4) using $e_{\text{lower}}(S_i)$ in Eq. (7) as the heuristic function. The implementation with Eq. (8) is similar, except for the additional computation of the spatial smoothness term. The implementation method follows from the work for the supervised column selection problem (Wan and Schweitzer 2021b).

To compute the heuristic value for a node, only the largest $O(k)$ singular values along with the trace are needed (see Eq. (7)). However, the singular values have to be calculated for every node, direct computation based on Eq. (7) is impractical. Note that the singular values of a matrix can be computed from the eigenvalues of the corresponding correlation matrix by taking the square root (e.g., (Golub and Van Loan 2013)). In our case, the singular values of X_i can be computed from the eigenvalues of $B_i = X_i X_i^T$.

Preprocessing

The EEG/MEG data X is of size $c \times \tau$, and the leadfield matrix L is of size $c \times m$, where the channel number c is much smaller than the number of sources m. In the initial step, we perform the eigendecomposition of the matrix $B = XX^T$. This gives: $B = UDU^T$, where the matrix U contains eigenvectors, and D is a diagonal matrix with the eigenvalues as the diagonal elements. Set $r = \min(c, \tau)$. We use the following D and P to replace X:

$$\begin{aligned} &\text{i. } D \in \mathbb{R}^{r \times r}; \\ &\text{ii. } P \in \mathbb{R}^{r \times c} = D^{\frac{1}{2}} U^T. \end{aligned} \tag{11}$$

This initial preprocessing can be performed efficiently by using randomized algorithms for matrix decompositions (e.g., (Halko, Martinsson, and Tropp 2011)). The time complexity is $O(c\tau r)$. The memory complexity is $O(cr)$.

Eigendecomposition at a Node

Instead of working on $B_i = X_i X_i^T$ at a node n_i, we use a related matrix H_i which has a special structure and the same eigenvalues as B_i, allowing efficient computation. Then, the singular values of X_i in Eq. (7) can be computed from the eigenvalues of H_i.

Lemma 5. Let Q_i be an orthonormal basis of S_i of size $c \times k_i$. Given D and P from Eq. (11), define:

$$H_i \in \mathbb{R}^{r \times r} = D - Z_i Z_i^T = D - \sum_{j=0}^{k_i - 1} z_j z_j^T, \tag{12}$$

where $Z_i = PQ_i$, $z_i = Pq_i$, and q_i is the ith column of Q_i. Then: H_i and B_i have the same nonzero eigenvalues.

See (Wan and Schweitzer 2021b) for proof. At each node, the complexity of computing the $O(k)$ eigenvalues is $O(crk)$ by using the randomized eigendecomposition algorithm (e.g., (Halko, Martinsson, and Tropp 2011)).

Complexity

Initially, we need to add m root nodes into the fringe list. The complexity is $O(mcrk)$. Suppose that a vertex on the brain mesh has $O(d)$ neighbors. In each iteration, there are $O(d)$ children to be created. Let T be the number of iterations. Then the overall time complexity is $O(mcrk + Tdcrk)$. The initial preprocessing time is ignored as m is bigger than τ. The value of T depends on the $l-$level neighborhood activation, d, and k. A larger l, a smaller d, and a smaller k lead to a smaller number of iterations T.

Experimental Results

We conducted experiments on both synthetic and real EEG data. In the experiments on the synthetic data, the proposed ESI-A^* algorithm was compared with the following algorithms: (i) deep learning approaches, which need to be trained by paired samples of EEG/MEG data X and source potentials Φ, including BiLSTM (Jiao et al. 2022), and Fully connected deep Neural Network (FNN) (Goodfellow, Bengio, and Courville 2016); (ii) well-known conventional ESI methods, which do not require training, including MxNE (implemented by MultiTaskLasso (MTL)) (Gramfort, Kowalski, and Hämäläinen 2012; Pedregosa et al. 2011), sLORETA (Pascual-Marqui 2002), dSPM (Dale et al. 2000), and MNE (Hämäläinen and Ilmoniemi 1994). In the experiments on the real EEG data, the proposed ESI-A^* algorithm was additionally compared with the results of DeepSIF (Sun et al. 2022), the surgical resection, and intracranial EEG defined seizure onset zone (SOZ).

Experiments on Synthetic Data

The brain forward model or the leadfield matrix was calculated using T1-MRI images from a 26-year-old male subject scanned at Massachusetts General Hospital, Boston, MA. We utilized a 128-channel BioSemi EEG cap layout, co-registered EEG channels with the head model using Brainstorm, and visualized using MNE-Python (Gramfort et al. 2014). The source space contains 1026 sources in each

Method	the activated area: 2 cm		the activated area: 4 cm	
	LE (std)	AUC (std)	LE (std)	AUC (std)
SNR = 40 dB				
MNE	38.6 (46.3)	0.92 (0.11)	38.4 (46.3)	0.89 (0.10)
sLORETA	27.7 (36.0)	0.94 (0.09)	26.3 (33.7)	0.91 (0.08)
dSPM	29.9 (19.4)	0.93 (0.08)	33.4 (21.2)	0.88 (0.09)
MTL	19.1 (09.0)	0.61 (0.07)	18.8 (09.3)	0.56 (0.02)
FNN	29.3 (27.5)	0.95 (0.12)	13.0 (21.8)	0.98 (0.08)
BiLSTM	33.9 (36.6)	0.94 (0.15)	14.8 (27.4)	0.98 (0.09)
Proposed	10.7 (04.9)	1.00 (0.00)	14.5 (05.9)	0.96 (0.05)
SNR = 30 dB				
MNE	61.3 (61.4)	0.86 (0.16)	60.9 (61.2)	0.82 (0.14)
sLORETA	46.0 (52.2)	0.89 (0.14)	45.5 (51.5)	0.85 (0.12)
dSPM	36.0 (28.8)	0.88 (0.14)	38.7 (29.1)	0.83 (0.12)
MTL	19.1 (09.0)	0.61 (0.07)	18.9 (09.7)	0.56 (0.02)
FNN	29.0 (27.7)	0.95 (0.12)	13.6 (23.5)	0.98 (0.08)
BiLSTM	34.1 (36.8)	0.93 (0.16)	14.8 (27.7)	0.98 (0.10)
Proposed	10.7 (04.9)	1.00 (0.00)	15.2 (06.8)	0.89 (0.07)
SNR = 20 dB				
MNE	100.6 (64.2)	0.75 (0.19)	102.2 (62.3)	0.71 (0.16)
sLORETA	87.1 (63.6)	0.79 (0.18)	90.4 (62.4)	0.74 (0.15)
dSPM	52.0 (43.9)	0.78 (0.18)	51.4 (41.2)	0.72 (0.15)
MTL	19.1 (09.3)	0.60 (0.06)	19.4 (10.3)	0.57 (0.03)
FNN	28.4 (27.2)	0.95 (0.12)	13.3 (20.4)	0.98 (0.09)
BiLSTM	33.0 (34.4)	0.94 (0.14)	15.4 (27.3)	0.97 (0.11)
Proposed	10.7 (05.0)	1.00 (0.00)	14.2 (06.9)	0.86 (0.06)
SNR = 10 dB				
MNE	122.1 (53.1)	0.62 (0.20)	123.1 (51.8)	0.60 (0.16)
sLORETA	116.4 (53.0)	0.62 (0.19)	120.1 (50.9)	0.60 (0.15)
dSPM	85.4 (54.5)	0.62 (0.19)	83.2 (54.0)	0.59 (0.14)
MTL	19.4 (10.4)	0.63 (0.07)	21.2 (12.9)	0.56 (0.03)
FNN	33.6 (33.4)	0.92 (0.16)	20.1 (32.1)	0.96 (0.12)
BiLSTM	37.7 (39.3)	0.91 (0.18)	20.9 (33.1)	0.95 (0.14)
Proposed	11.1 (05.1)	0.99 (0.05)	15.9 (08.5)	0.87 (0.06)

Table 1: Performance comparison with different SNR levels.

hemisphere (2052 in total), resulting in a leadfield matrix L of size 128×2052. We used an autoregressive model with an order of 5 to generate the time series (Haufe and Ewald 2016). We randomly selected locations in the cortex to be activated. To simulate the source extent pattern, we also activated the first and/or second levels of neighbors. The diameter of the activated area with the 1-level neighborhood activation is approximately 2 cm (about 7 vertices), and the diameter of the activated area with the 2-level neighborhood activation is approximately 4 cm (about 19 vertices).

The forward model in Eq. (1) was used to generate the scalp EEG data X with additive channel noise specified under different signal-to-noise ratio (SNR) settings (SNR=40, 30, 20, and 10 dB). SNR is defined as the ratio of the signal power P_{signal} to the noise power P_{noise}: SNR $= 10\log(P_{\text{signal}}/P_{\text{noise}})$. For each combination of the SNR setting and neighborhood level, we randomly picked 20 locations on the brain mesh to conduct the source reconstruction. We set the length of EEG data in each experiment to be 1 second with a 100 Hz sampling rate; thus, the dimension of EEG data X is 128 by 100. In total, there were 160 experiments (X and Φ pairs): 4 (SNRs) $\times$ 2 (neighborhoods) $\times$ 20 (locations). These data sets were used for evaluating the performance of the algorithms. For deep learning methods, additional training data was generated with SNR=20 by randomly activating different source locations. We used a total training data of 200,000 pairs of X and Φ.

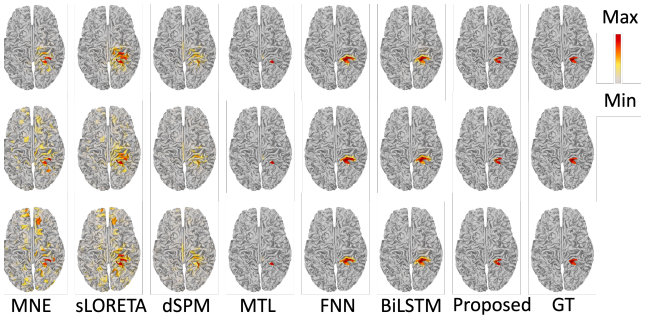

Figure 3: Source activation reconstruction comparison under different SNRs. Top row: 40 dB, middle row: 20 dB, and bottom row: 10 dB. The size of the activated area is 2 cm.

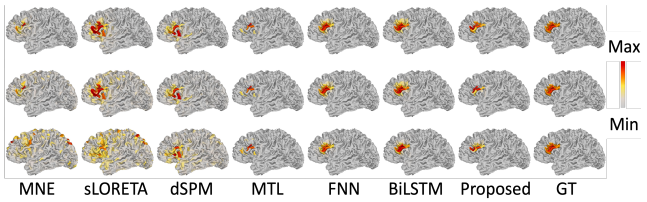

Figure 4: Source activation reconstruction comparison under different SNRs. Top row: 40 dB, middle row: 20 dB, and bottom row: 10 dB. The size of the activated area is 4 cm.

Experimental settings. For the BiLSTM, the hidden layer contains 3200 LSTM units, connecting the input and output layers. The FNN has an input layer with a dimension of 128, and 3 hidden layers with 1280, 1280, and 2560 neurons in each layer, and the output layer's dimension is 2052. The MNE, sLORETA and dSPM algorithms were used with the default settings from MNE-python (Gramfort et al. 2014). We applied the MultiTaskLasso (MTL) implementation of MxNE from the scikit-learn library (Pedregosa et al. 2011), using ℓ_1 in the spatial domain and ℓ_2 in the temporal domain. Thus, $\ell_{1,2}$ norm was used for MTL. The ESI-A^* algorithm was optimized on (4) with k=7 when the activated area size is 2 cm and k=17 when the activated area size is 4 cm. The reconstruction results from all algorithms and the ground truth (GT) based on one activated area are presented, which is a typical activation pattern in focal epilepsy patients (Flanagan, Badawy, and Jackson 2014; Sun et al. 2022).

The experiments were conducted on a Windows PC with i9 CPUs and 64 GB memory, and the deep learning models were trained using an NVIDIA V100 with 32 GB memory.

Evaluation criteria. We quantitatively evaluated algorithms based on two metrics: (i) *Localization Error (LE)*: It is widely used to evaluate the performance of algorithms for the ESI problem (Sohrabpour et al. 2020), measuring the geodesic distance between two activated areas using the Dijkstra shortest path algorithm. (ii) *Area Under Curve (AUC)*: It is particularly useful to characterize the overlap between two activated areas. A better algorithm should have a lower LE value and a higher AUC value.

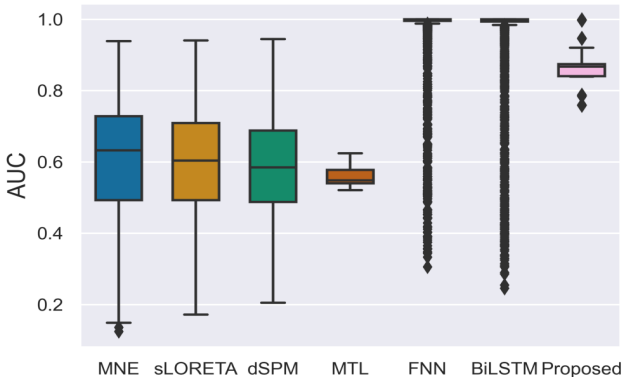

Figure 5: Boxplots when SNR: 10dB and the area size: 4cm.

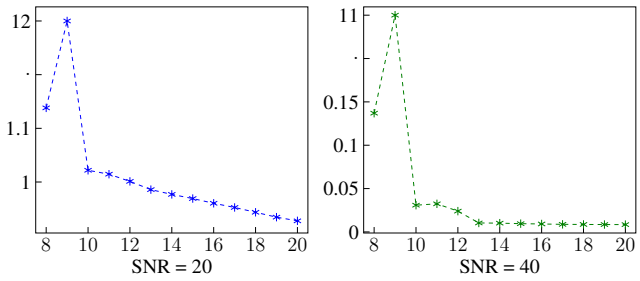

Figure 6: The change in error (Y-axis) as a function of k (X-axis). The true number of activated vertices is 19.

Table 1 presents the detailed comparison results. Figure 3 and Figure 4 show the source reconstruction comparison of the conventional methods (MNE, sLORETA, dSPM, and MTL), the deep learning methods (FNN and BiLSTM), and the proposed algorithm (ESI-A^*). The proposed algorithm, which did not require training, compared favorably with the deep learning methods that required tremendous training data (200,000 samples). When the activated area size is 4 cm and SNR = 30/20/10 dB, the AUC values of the proposed algorithm deteriorated slightly compared to the FNN and BiLSTM. However, the reconstructed sources from FNN and BiLSTM presented a much larger variance (long tails in the boxplots in Figure 5), indicating that the reconstruction sometimes can be far away from the true activated area. Compared to other conventional methods, the proposed algorithm could render more accurate reconstructions.

The parameter k. The proposed algorithm requires an estimate of the number of vertices in an activated area. We investigated the change of the optimization error (4) as a function of k (Figure 6). The true number of activated vertices is 19 (the activated area of size 4 cm). The results showed that when $k \geq 14$, the proposed algorithm can identify the correct activated vertices. As expected, when SNR is low (e.g., 20 dB), the error gradually decreases after $k=10$. When SNR is high (e.g., 40 dB), the error tends to be 0 after $k=13$.

Evaluations on Real Epilepsy Data

The proposed algorithm was validated on a cohort of 20 patients with drug-resistant epilepsy who underwent resection surgery with seizure-free outcomes for at least one year (Sun et al. 2022). The EEG data and MRI images were collected at the Mayo Clinic, Rochester, MN. The outcome of the surgical intervention was scored based on the International League Against Epilepsy (ILAE) system by physicians with a follow-up period of 20 $\pm$ 9 months. The number of channels is 75 after removing a reference electrode. Interictal spikes were extracted from the EEG data, and an averaged spike was used for seizure onset zone (SOZ) reconstruction.

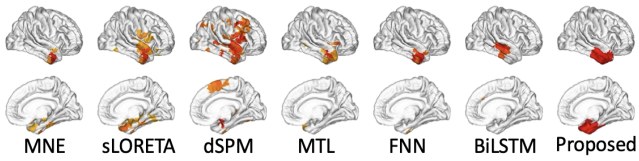

Figure 7: Comparison of reconstructed epileptogenic zones.

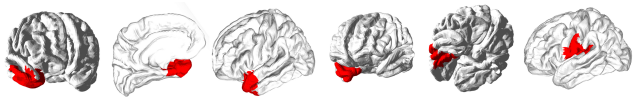

Figure 8: Epileptogenic zones for six patients (#2, #3, #7, #14, #15, and #17) detected by ESI-A^*. The results of the DeepSIF and the "ground truth" (the resection and seizure onset zone) can be found in Figure S14 of Sun et al. (2022).

The reconstructed results for patient #2 (Sun et al. 2022) are shown in Figure 7. The ground truth can be found in Figure S14 and Figure 5.A of Sun et al. (2022). The proposed algorithm detected the SOZ and the resection region accurately. Additional reconstruction results for additional patients using the proposed method with k=20 are presented in Figure 8. The ground truth and the results of DeepSIF can be found in Figure S14 of Sun et al. (2022). The identified regions by the proposed ESI-A^* algorithm have a high concordance with the resection and SOZ. For patient #17, the proposed algorithm succeeded in detecting the ground truth region, while the result given by DeepSIF was less accurate.

Conclusion

In neuroscience, reconstructing the brain source activation is fundamental for understanding the brain mechanism and disorders. We propose a combinatorial search approach by exploiting the graph-structured sources defined on the brain mesh, and the proposed algorithm enjoys a provable optimality guarantee. This new algorithm to address the ESI problem showed good concordance in reconstructing the underlying source activation in both simulated studies and epileptogenic area detection for epilepsy patients.

The proposed algorithm requires an estimate of the number of vertices in an activated area, allowing a series of potential solutions to characterize the possible SOZs. Different potential solutions, along with the corresponding EEG data fitting errors and activated sizes, will help neurosurgeons make better decisions. The proposed algorithm needs to be further validated on real patient data.

Acknowledgments

G. Wan would like to thank her advisor, Dr. Yevgeniy R. Semenov, for his support in this study.

References

Babadi, B.; Obregon-Henao, G.; Lamus, C.; Hämäläinen, M. S.; Brown, E. N.; and Purdon, P. L. 2014. A subspace pursuit-based iterative greedy hierarchical solution to the neuromagnetic inverse problem. *NeuroImage*, 87: 427–443.

Costa, F.; Batatia, H.; Chaari, L.; and Tourneret, J.-Y. 2015. Sparse EEG source localization using Bernoulli laplacian priors. *IEEE Transactions on Biomedical Engineering*, 62(12): 2888–2898.

Cuffin, B. N.; and Cohen, D. 1979. Comparison of the magnetoencephalogram and electroencephalogram. *Electroencephalography and clinical neurophysiology*, 47(2): 132–146.

Dale, A. M.; Liu, A. K.; Fischl, B. R.; Buckner, R. L.; Belliveau, J. W.; Lewine, J. D.; and Halgren, E. 2000. Dynamic statistical parametric mapping: combining fMRI and MEG for high-resolution imaging of cortical activity. *neuron*, 26(1): 55–67.

Ding, L.; and He, B. 2008. Sparse source imaging in electroencephalography with accurate field modeling. *Human brain mapping*, 29(9): 1053–1067.

Ding, L.; Wilke, C.; and *et al.* 2007. EEG source imaging: correlate source locations and extents with ECoG and surgical resections in epilepsy patients. *Journal of clinical neurophysiology: official publication of the American Electroencephalographic Society*, 24(2): 130.

Flanagan, D.; Badawy, R. A.; and Jackson, G. D. 2014. EEG–fMRI in focal epilepsy: local activation and regional networks. *Clinical Neurophysiology*, 125(1): 21–31.

Golub, G. H.; and Van Loan, C. F. 2013. *Matrix computations*. JHU press.

Goodfellow, I.; Bengio, Y.; and Courville, A. 2016. *Deep learning*. MIT press.

Gramfort, A.; Kowalski, M.; and Hämäläinen, M. 2012. Mixed-norm estimates for the M/EEG inverse problem using accelerated gradient methods. *Physics in medicine and biology*, 57(7): 1937.

Gramfort, A.; Luessi, M.; Larson, E.; Engemann, D. A.; Strohmeier, D.; Brodbeck, C.; Parkkonen, L.; and Hämäläinen, M. S. 2014. MNE software for processing MEG and EEG data. *Neuroimage*, 86: 446–460.

Gramfort, A.; Strohmeier, D.; Haueisen, J.; Hämäläinen, M. S.; and Kowalski, M. 2013. Time-frequency mixed-norm estimates: Sparse M/EEG imaging with non-stationary source activations. *NeuroImage*, 70: 410–422.

Guo, Y.; Jiao, M.; Wan, G.; Xiang, J.; Wang, S.; and Liu, F. 2022. EEG Source Imaging using GANs with Deep Image Prior. In *2022 44th Annual International Conference of the IEEE Engineering in Medicine & Biology Society (EMBC)*, 572–575. IEEE.

Halko, N.; Martinsson, P. G.; and Tropp, J. A. 2011. Finding structure with randomness: Probabilistic algorithms for constructing approximate matrix decompositions. *SIAM Review*, 53(2): 217–288.

Hämäläinen, M. S.; and Ilmoniemi, R. J. 1994. Interpreting magnetic fields of the brain: minimum norm estimates. *Medical biological engineering and computing*, 32(1): 35–42.

Hart, P. E.; Nilsson, N. J.; and Raphael, B. 1968. A formal basis for the heuristic determination of minimum cost paths. *IEEE transactions on Systems Science and Cybernetics*, 4(2): 100–107.

Haufe, S.; and Ewald, A. 2016. A simulation framework for benchmarking EEG-based brain connectivity estimation methodologies. *Brain topography*, 1–18.

Haufe, S.; Tomioka, R.; Dickhaus, T.; Sannelli, C.; Blankertz, B.; Nolte, G.; and Müller, K.-R. 2011. Large-scale EEG/MEG source localization with spatial flexibility. *NeuroImage*, 54(2): 851–859.

He, B.; and Ding, L. 2013. Electrophysiological mapping and neuroimaging. In *Neural engineering*, 499–543. Springer US.

He, B.; Shah, S.; Maung, C.; Arnold, G.; Wan, G.; and Schweitzer, H. 2019. Heuristic search algorithm for dimensionality reduction optimally combining feature selection and feature extraction. In *Proceedings of the AAAI conference on artificial intelligence*, volume 33, 2280–2287.

He, B.; Sohrabpour, A.; Brown, E.; et al. 2018. Electrophysiological source imaging: A noninvasive window to brain dynamics. *Annu. review of biomedical engineering*.

Huettel, S. A.; Song, A. W.; McCarthy, G.; et al. 2004. *Functional magnetic resonance imaging*, volume 1. Sinauer Associates Sunderland.

Iida, K.; and Otsubo, H. 2017. Stereoelectroencephalography: indication and efficacy. *Neurologia medico-chirurgica*, 57(8): 375–385.

Jiao, M.; Wan, G.; Guo, Y.; Wang, D.; Liu, H.; Xiang, J.; and Liu, F. 2022. A Graph Fourier Transform Based Bidirectional Long Short-Term Memory Neural Network for Electrophysiological Source Imaging. *Frontiers in Neuroscience*, 16: 867466–867466.

Keene, D.; Whiting, S.; and Ventureyra, E. 2000. Electrocorticography. *Epileptic Disorders*, 2(1): 57–64.

Liu, F.; Rosenberger, J.; Lou, Y.; Hosseini, R.; Su, J.; and Wang, S. 2017. Graph regularized EEG source imaging with in-class consistency and out-class discrimination. *IEEE Transactions on Big Data*, 3(4): 378–391.

Liu, F.; Wan, G.; Semenov, Y. R.; and Purdon, P. L. 2022. Extended electrophysiological source imaging with spatial graph filters. In *International Conference on Medical Image Computing and Computer-Assisted Intervention*, 99–109. Springer.

Liu, F.; Wang, L.; Lou, Y.; Li, R.-C.; and Purdon, P. L. 2020. Probabilistic structure learning for EEG/MEG source imaging with hierarchical graph priors. *IEEE transactions on medical imaging*, 40(1): 321–334.

Liu, F.; Wang, S.; Qin, J.; Lou, Y.; and Rosenberger, J. 2018. Estimating latent brain sources with low-rank representation and graph regularization. In *Brain Informatics: International Conference, BI 2018, Arlington, TX, USA, December 7–9, 2018, Proceedings 11*, 304–316. Springer.

Marshall, A. W.; Olkin, I.; and Arnold, B. C. 2011. *Inequalities: Theory of Majorization and Its Applications*. Springer, second edition.

Muehllehner, G.; and Karp, J. S. 2006. Positron emission tomography. *Physics in Medicine & Biology*, 51(13): R117.

Pascual-Marqui, R. D. 2002. Standardized low-resolution brain electromagnetic tomography (sLORETA): technical details. *Methods Find Exp Clin Pharmacol*, 24(Suppl D): 5–12.

Pedregosa, F.; Varoquaux, G.; Gramfort, A.; Michel, V.; Thirion, B.; Grisel, O.; Blondel, M.; Prettenhofer, P.; Weiss, R.; Dubourg, V.; et al. 2011. Scikit-learn: Machine learning in Python. *the Journal of machine Learning research*, 12: 2825–2830.

Phillips, C.; Rugg, M. D.; and Friston, K. J. 2002. Anatomically informed basis functions for EEG source localization: combining functional and anatomical constraints. *NeuroImage*, 16(3): 678–695.

Pirondini, E.; Babadi, B.; Obregon-Henao, G.; Lamus, C.; Malik, W. Q.; Hämäläinen, M. S.; and Purdon, P. L. 2017. Computationally efficient algorithms for sparse, dynamic solutions to the EEG source localization problem. *IEEE Transactions on Biomedical Engineering*, 65(6): 1359–1372.

Qin, J.; Liu, F.; Wang, S.; and Rosenberger, J. 2017. EEG Source Imaging based on Spatial and Temporal Graph Structures. In *International Conference on Image Processing Theory, Tools and Applications*.

Sohrabpour, A.; Cai, Z.; Ye, S.; Brinkmann, B.; Worrell, G.; and He, B. 2020. Noninvasive electromagnetic source imaging of spatiotemporally distributed epileptogenic brain sources. *Nature communications*, 11(1): 1–15.

Sohrabpour, A.; and He, B. 2021. Exploring the extent of source imaging: Recent advances in noninvasive electromagnetic brain imaging. *Current Opinion in Biomedical Engineering*, 18: 100277.

Sun, R.; Sohrabpour, A.; Worrell, G. A.; and He, B. 2022. Deep neural networks constrained by neural mass models improve electrophysiological source imaging of spatiotemporal brain dynamics. *Proceedings of the National Academy of Sciences*, 119(31): e2201128119.

Uutela, K.; Hämäläinen, M.; and Somersalo, E. 1999. Visualization of magnetoencephalographic data using minimum current estimates. *NeuroImage*, 10(2): 173–180.

Wan, G. 2021. *AI Inspired Algorithms for Several Combinatorial Optimization Problems in Data Science*. Ph.D. thesis, The University of Texas at Dallas.

Wan, G.; and Schweitzer, H. 2021a. Accelerated combinatorial search for outlier detection with provable bound on sub-optimality. In *Proceedings of the AAAI Conference on Artificial Intelligence*, volume 35, 12436–12444.

Wan, G.; and Schweitzer, H. 2021b. Heuristic Search for Approximating One Matrix in Terms of Another Matrix. In *International Joint Conferences on Artificial Intelligence (IJCAI)*, 1600–1606.

Wan, G.; and Schweitzer, H. 2021c. A Lookahead Algorithm for Robust Subspace Recovery. In *2021 IEEE International Conference on Data Mining (ICDM)*, 1379–1384.

Xu, F.; Liu, K.; Yu, Z.; Deng, X.; and Wang, G. 2021. EEG extended source imaging with structured sparsity and L1-norm residual. *Neural Computing and Applications*, 33(14): 8513–8524.

Yang, Y.; Aminoff, E.; Tarr, M.; and Robert, K. E. 2016. A state-space model of cross-region dynamic connectivity in MEG/EEG. In *Advances in Neural Information Processing Systems*, 1234–1242.